Experimental overview of Ni+Ni collisions at 32 MeV/nucleon: Discriminant analysis and duality in the decay modes of a fusionlike system

P. Lautesse,[1] A. M. Maskay,[1] E. Gerlic,[1] P. Désesquelles,[2] J. L. Laville,[3] O. Lopez,[4] B. Borderie,[2] R. Dayras,[5] A. Demeyer,[1] D. Durand,[4] J. D. Frankland,[3] E. Galichet,[2,6] D. Guinet,[1] B. Guiot,[3] N. Le Neindre,[3] J. Marie,[4] L. Nalpas,[5] M. Pârlog,[7] M. Pichon,[4] M. F. Rivet,[2] E. Rosato,[8] R. Roy,[9] C. Schmitt,[1,3] B. Tamain,[4] E. Vient,[4] M. Vigilante,[8] C. Volant,[5] and J. P. Wieleczko[3]

(INDRA Collaboration)

[1]*Institut de Physique Nucléaire, IN2P3-CNRS et Université, F-69622 Villeurbanne, France*

[2]*Institut de Physique Nucléaire, IN2P3-CNRS, F-91406 Orsay Cedex, France*

[3]*GANIL, CEA et IN2P3-CNRS, B.P. 5027, F-14076 Caen Cedex, France*

[4]*LPC, IN2P3-CNRS, ENSI-Caen et Université, F-14050 Caen Cedex, France*

[5]*DAPNIA/SPhN, CEA/Saclay, F-91191 Gif sur Yvette, France*

[6]*Conservatoire National des Arts et Métiers, F-75141 Paris Cedex 03, France*

[7]*National Institute for Physics and Nuclear Engineering, Bucharest-Măgurele, Romania*

[8]*Dipartimento di Scienze Fisiche e Sezione INFN, Università di Napoli "Federico II," I-80126 Napoli, Italy*

[9]*Laboratoire de Physique Nucléaire, Université Laval, Québec, Canada*

(Received 19 November 2003; published 15 March 2005)

^{58}Ni+^{58}Ni collisions at 32 MeV/nucleon have been studied with the 4π multidetector INDRA. The evolution from binary (dissipative) collisions to a fusionlike process is evidenced with decreasing impact parameter throughout a set of experimental observables within a discriminant analysis. Preequilibrium effects and characteristics of a single-source emission are discussed. A coexistence (bimodality) between two decay mechanisms is pointed out and examined in the context of a multiple-fragment (particle) emission.

DOI: 10.1103/PhysRevC.71.034602 PACS number(s): 25.70.Lm, 25.70.Pq

I. INTRODUCTION

Reaction processes implying the formation and decay of a hot composite nucleus including most of the incident nucleons constitute a non-negligible contribution to the cross section of central collisions between heavy ions around Fermi energy [1–11]. The concerned incident energy range, often referred to as "intermediate energies," runs from over 20 up to 100 MeV/nucleon, where individual nucleon-nucleon collision effects overcome mean-field effects. In that wide energy domain, a beam energy value of 32 MeV/nucleon—close to the Fermi energy—appears to be well suited to produce these intermediate subsystems, since it is well above the Coulomb regime while not being too high for the aforementioned effects to be dominant. At that energy, it is well known that the complete fusion process, which ends up in a cold heavy residue storing the whole initial mass and some evaporation particles, has vanished [5,6] and been replaced by collisions leading to dominant multisource events. Nevertheless, the formation of hot composite subsystems has been evidenced in various experimental data involving central collisions, mainly in heavy (e.g., Xe+Sn [3]) and very heavy (e.g., Au+Au [10], Gd+U [9]) systems. They appear to be highly excited—typically above 5 MeV/nucleon—and their sizes are close to the total incident mass (projectile + target nuclei) except for the fraction emitted in the preequilibrium phase. Above an excitation energy of about 3–5 MeV/nucleon, their decay occurs with a relatively abundant production of fragments with charge $Z \geqslant 3$. Moreover, these subsystems appear to have reached a high degree of thermalization since many observables seem to be mainly driven by statistical decay. Therefore, it is fundamental that we understand the reaction mechanisms that lead to such an extreme situation: How is it possible to create an intermediate subsystem that concentrates almost the whole initial mass and presumably reaches thermal equilibrium in a rather short time? Do we deal with a more and more unstable incomplete fusion system or with a completely different mechanism?

To analyze this hot source, it is necessary to eliminate nonequilibrated components that might contaminate the exit channel. Indeed, dynamical models [12] suggest that out-of-equilibrium nucleon emission may occur at various stages of the reaction, as confirmed by experiment [13]; such processes are often referred to as preequilibrium emission [4,14]. One aspect of preequilibrium emission has been recently evidenced as a "spray" [7], which implies forward production of not only light particles but also light fragments. A deeper and more realistic overall insight into these processes requires exclusive experiments performed with a multidetector array and a good discrimination of single-source events. Thus, a specific procedure able to isolate the single-source subset from major contributions of multisource events is necessary. Such a procedure has been widely discussed in a previous paper [15], where the quality of the resulting sample of single-source events has been shown. We even deduced a reliable "fusionlike" cross section of 170 ± 20 mb for the ^{58}Ni+^{58}Ni reaction at 32 MeV/nucleon [2,15].

In the present paper, we report on an investigation of such reaction mechanisms including a persistent fusionlike process in these 32 MeV/nucleon ^{58}Ni+^{58}Ni collisions. One of the

underlying purposes is to determine to what extent the system has forgotten the entrance channel, i.e., how far this fusionlike source might be considered as a hot composite nucleus. After a short description of the experimental procedure involving the multidetector INDRA (Sec. II), we shall study in a more refined way the performances of the new discriminant variable d_{625} throughout the experimental evolution of various observables in order to characterize the single-source events selected among dominant polysource ones (Sec. III). Then, the hypothesis of the fusionlike nucleus at thermal equilibrium will be verified and the preequilibrium emission characterized (Sec. IV). Finally Sec. V will be devoted to the decay properties of the hot source and followed by conclusions in Sec. VI.

II. EXPERIMENTAL DETAILS

The experiment was performed at Grand Accélérateur National d'Ions Lourds (GANIL) with the $^{58}Ni^{24+}$ beam at 32 MeV/nucleon impinging on a 179-μg/cm^2 ^{58}Ni target. Events were recorded by the INDRA charged products multidetector. As INDRA's characteristics are exhaustively described in a technical paper [16], we only recall here its main features. INDRA is an ensemble of 336 detection cells arranged in 17 rings; the first one ($2^\circ-3^\circ$) is a phoswich array of plastic scintillators. Rings 2–9 (i.e., for polar angles ranging from 3° to 45°) consist of three level telescopes including an ionization chamber (IoCh) followed by a solid-state silicon detector (Si) and a cesium iodide scintillator, CsI (Tl). The medium and backward angular range (45°–176°) is restricted to IoCh/CsI moduli. The multiplicity triggering condition was set to a minimum of four modules firing per event ($M \geqslant 4$) in order to eliminate the most peripheral collisions. The whole INDRA device provides detection, identification, and an energy measurement with a 90% of 4π geometrical efficiency.

Figure 1 presents the diagram of the total reconstructed momentum $P_{\rm tot} = \sum_{j=1}^{\rm Mult} m_j |v_j|$, where j is the fragment (or light particle) number in a given event with multiplicity Mult, versus the total charge $Z_{\rm tot}$ detected by INDRA. One sees that quite full efficiency is achieved, provided we use a subset of "complete" events as in zone γ, characterized by a performant detection involving $\geqslant 80\%$ of the initial charge $Z_{\rm ini}$ and momentum $P_{\rm ini}$. The α and β zones correspond to events when a large part of the charge and/or momentum is missed. The present study is then restricted to that subset γ of complete events, excluding the most peripheral collisions, which represents about 13% of the detected events.

Figure 2 displays a set of charge-versus-energy maps for each identification level allowed by INDRA. They illustrate the three kinds of ΔE-E telescope contributions. These maps exhibit the charge-energy plots for fragments detected over the whole 4π acceptance. Particle and fragment identification is obtained on the full charge/energy range concerned by these Ni+Ni collisions at 32 MeV/nucleon. The left column, related to IoCh/Si maps, is devoted to slow (mostly heavy) fragments detected at forward angles ($\leqslant 45^\circ$). The middle column displays Si/CsI maps, for faster and lighter fragments, also detected at forward angles. Finally, the right column displays IoCh/CsI maps, with fragments detected at larger

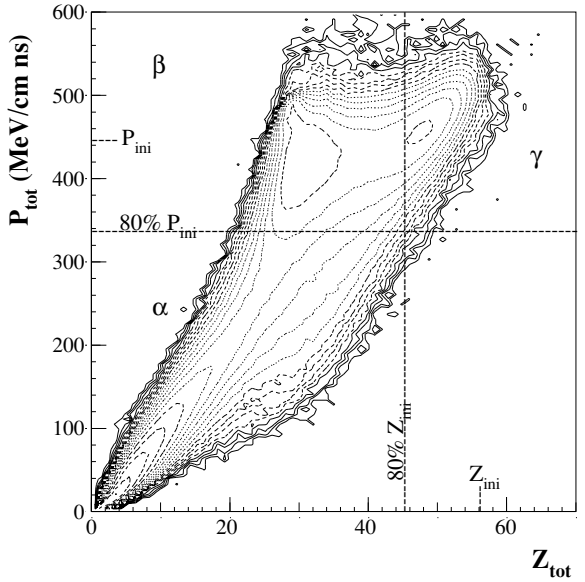

FIG. 1. Total momentum versus total charge detected by INDRA for the ^{58}Ni+^{58}Ni system at 32 MeV/nucleon. $Z_{\rm ini}$ and $P_{\rm ini}$ are the initial values of total charge and momentum (axis z with a logarithmic scale). Limits of γ zone are shown to represent the selected set of complete events (see text).

angles ($\geqslant 45^\circ$). The light products, $Z = 1$–4 (not shown), are isotopically identified by the Si/CsI telescopes or the CsI alone.

Looking at Fig. 2 another way, the top row is devoted to "pure single-source events," the middle row to "pure polysource events," and the bottom one to the whole sample of complete events under study. One can see that all products are very well characterized in charge and energy. The single-source and polysource selections are made explicit in the next section. We already stress the very different pattern of the charge-energy maps of the top row (single-source events) compared with the two other rows.

III. SINGLE-SOURCE DISCRIMINATION: EXPERIMENTAL OVERVIEW

In this section, we report on a set of observables directly built up from the experimental data, with the aim of establishing the capability of the discriminant analysis (DA) [17] method to disentangle the various mechanisms involved in a selected sample of events. The ultimate purpose is to study the characteristics of the fusionlike system formed in the reaction.

In Sec. III A, we briefly review the DA method involving multivariate moments and used to separate the single-source component from the polysource components. To evaluate the discrimination efficiency of the procedure, one needs to go through a simulation stage for which we used the event generator SIMON [18,19]. It provides a realistic simulation of heavy-ion collisions at intermediate energies. The SIMON code describes the overall reaction process, including the entrance channel dynamics over the full impact parameter range, thus leading to either a binary or a fused system

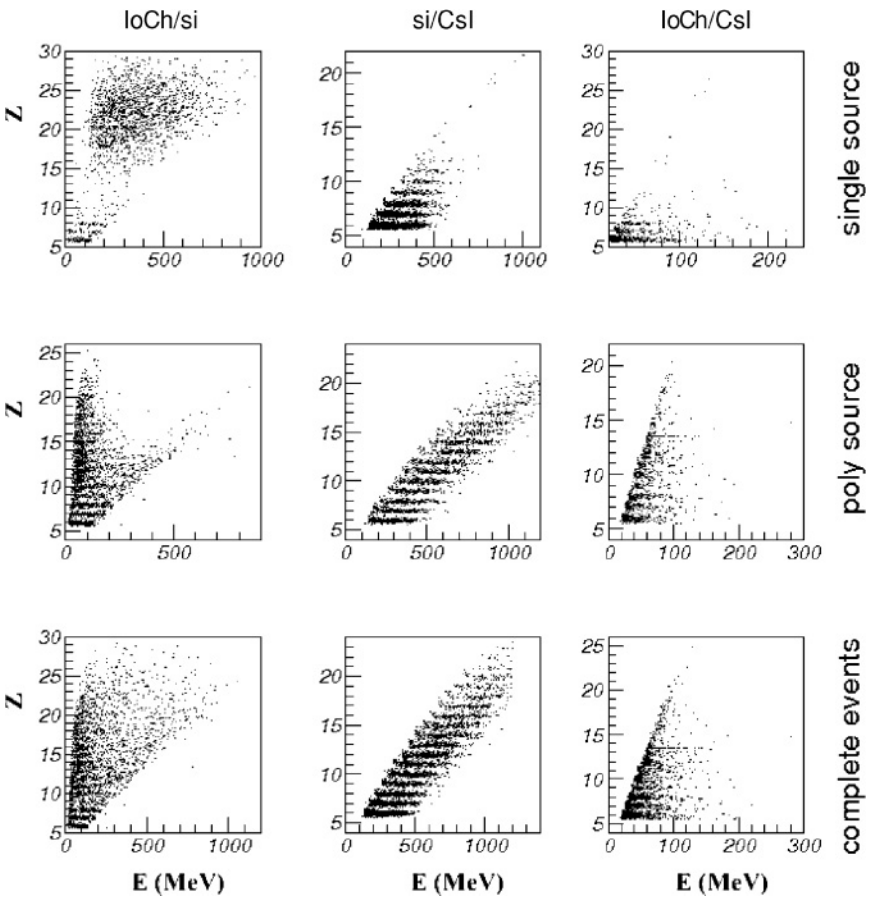

FIG. 2. Charge ($Z > 4$) versus energy maps for each Z identification level as described in the text. The three columns stand for the three kinds of ΔE-E telescope arrangements, while the three rows display the three types of events, i.e., complete events and complete events with single-source or polysource selection (see text).

formation within a sharp cutoff description. The decay of the resulting subsystems is described within a sequential emission framework. Outgoing fragments and particles are driven in the final Coulomb field. The code has been shown in [2,15] to provide a qualitative agreement with the present experimental distributions of static, kinetic, and shape observables, therefore constituting a good tool for developing such a discriminant analysis procedure. The generated events are finally filtered according to the multidetector response function. Finally the experimental events are sorted out into four classes according to the resulting discriminant variable d_{625}. Then static and kinematic experimental observables are analyzed for those classes in Sec. III B.

A. Discriminant analysis method and resulting d_{625} variable

This original method for separating a single-source component from other contributions has been recently developed [2,15]. It is applied here to the whole set of complete events as defined above and follows a two-step procedure:

i. A subspace describing the experimental information in an optimum way is chosen. The basis vectors of this subspace are the so-called multivariate moments, defined as

$$M_{jklm} = \sum_{\nu=1}^{\mathrm{Mult}} E_A^j(\nu) E_x^k(\nu) E_y^l(\nu) E_z^m(\nu),$$

where ν is the fragment (or light particle) number in a given event with multiplicity Mult. The mass energy of the ν^{th} product is noted as E_A; and E_x, E_y, E_z are defined by $E_i = E_{\mathrm{kin}} \cos\theta_i$, where E_{kin} is the kinetic energy in the laboratory frame, θ_i the laboratory angle between the hit detector and axis i with $i \in \{x, y, z\}$, and z the beam axis.

ii. The most suitable linear combination of these multivariate moments to provide the best discrimination between single and polysource events is searched for using a DA technique.

The best deduced linear combination of the 625 first quadrimoments $\{M_{jklm\in\{0,\ldots,4\}}\}$ is called the d_{625} variable (with $d_{625} = \sum_{(j,k,l,m)=0}^{4} \alpha_{jklm} M_{jklm}$). It can be shown that the moments known up to high enough (j, k, l, m) orders allow one to reconstruct the initial fragment characteristics. In our case, 625 was checked as the number of multivariate moments needed to obtain the amount of information required to significantly describe the whole set of data. It is worth remembering that the discriminant power and overlap parameters of this d_{625} variable have proved to be much more efficient compared with the commonly used selection variables such as the isotropy ratio or the flow angle. This is true at least regarding the Ni+Ni system at 32 MeV/nucleon. Furthermore, we emphasize that a larger event sample is obtained in most cases when the event selection is performed with the d_{625} variable instead of the usual global variables.

B. Evolution of some experimental characteristics of the 32 MeV/nucleon Ni+Ni collisions as a function of the d_{625} variable value

In this section, we show that the DA procedure is a powerful tool for characterizing reaction mechanisms evolving from fusionlike to binarylike collisions. We study this evolution through a set of significant experimental individual and global variables.

We have already shown in [15] that the experimental single-source sample belongs to a low-impact parameter range ($b \leqslant 3$ fm) compared to the maximum experimental value of 7.5 fm imposed by the complete event selection, the geometric value being $b_{\max} = 9.94$ fm. However, although a separation between the single/polysource components was clearly observable, the analysis pointed out that even in the central region of impact parameters (1–3 fm) where the single-source component was dominant, some contamination with polysource events was still present.

In the present work, the optimized experimental d_{625} distribution is divided, as shown in Fig. 3 (top row), into four adjacent regions (a)–(d) ranging from a pure single-source sample (a) to a pure polysource one (d). Bins (b) and (c) are different mixtures of both contributions. A pure class is defined as a sample being contaminated by less than 3% of events of the other class. The limits of these cuts are deduced, as presented in [15], from a detailed study of the experimental d_{625} two-component distribution, fitted with the sum of two Gaussians. Each of these four slices amounts to ∼50% of the relevant Gaussian.

Figures 3 and 4 display the evolution of some typical static and kinetic variables gated by these d_{625} cuts.

1. Static variables

Figure 3 is concerned with the evolution of some static variables, charge Z, $Z_{\max}$, $Z_{\max-1}$, and asymmetry distributions, as a function of the d_{625} intervals.

The *charge distributions f(Z)* show a clear evolution from column (a_1) to (d_1). The pure single source in (a_1) seems to consist essentially of events including, on the one hand, relatively heavy fragments peaking around $Z \sim 22$ and extending up to $Z \sim 35$ which could be assimilated to incomplete fusion residues and, on the other hand, numerous light products. A pronounced depletion of fragments with $Z \sim 10$–15 is clearly observed in (a_1) and progressively vanishes from (b_1) to (d_1) regions. Pure polysource charge distributions appear, forming a plateau between $Z \sim 6$ and $Z \sim 20$, followed by a tail extending up to $Z \sim 30$.

The distributions of $Z_{\max}$ for each event, (a_2) to (d_2), reinforce the previous observations. From the curve (a_2), $Z_{\max}$ points clearly at ∼22, the distribution extending from ∼12 to ∼32, compared to $Z_{\text{tot}} = 56$, suggesting a high energy dissipation. Then for (d_2) the $Z_{\max}$ mean value decreases to $\langle Z_{\max} \rangle \sim 14$, with a distribution extending from ∼6 to ∼25. This latter experimental curve indeed suggests two main Gaussian contributions, i.e., a dominant one with $\langle Z_{\max} \rangle \sim 12$ only and a smaller one with $\langle Z_{\max} \rangle \sim 18$, thus reflecting clearly two classes of events in the (d_2) cut. Note that the dominant contribution corresponds to more dissipative events than the other one.

The *charge correlation* between the two heaviest fragments of the events is displayed from (a_3) to (d_3). In the (d_3) sample, they appear mainly concentrated along the line $Z_{\max-1} \sim Z_{\max}$, as expected for dominant binarylike collisions of a symmetric system. On the opposite, the single-source sample (a_3) presents a bulk which corresponds to expected residues but with most values of $Z_{\max}$ running globally from ∼20 to ∼27, combined with lighter fragments belonging to two islets pointing around $Z \sim 3$ and 6. Note that the $Z_{\max-1}$ value never exceeds ∼12. These features reflect once more the probable formation of a hot fusionlike nucleus, since the $Z_{\max}$ residuelike has a relatively small size and is accompanied by numerous light fragments and/or particles. In addition, one can note the significant gradual vanishing, from single-source to polysource samples, of the very light $Z_{\max-1}$ products in the first islet ($Z < 4$).

The *charge asymmetry* variable [20], which yields a more refined insight into the contents of an event, is defined as

$$\text{Asym}_{123} = \sqrt{\sum_{n=1}^{3} \left(Z_{\max_n} - \langle Z \rangle\right)^2} (\sqrt{6}\langle Z \rangle)^{-1},$$

where $Z_{\max_n}$ are the charges of the three heaviest products in an event ($Z_{\max_1} \geqslant Z_{\max_2} \geqslant Z_{\max_3}$), and $\langle Z \rangle$ is their mean value. The variable Asym_{123} reflects the symmetry of the charge partition. Values close to 0 stand for nearly equal sizes while values close to 1 imply a heavy fragment plus two light charged products. The medium case ($\text{Asym}_{123} \sim 0.5$) then corresponds to the combination of two close size fragments and a light particle. The evolution of the variable Asym_{123} is shown in the bottom part of Fig. 3 from (a_4) to (d_4). In the polysource case (d_4), the Asym_{123} extends up to ∼0.5 and the strong narrow peak pointing at ∼0.45 corresponds to a binarylike dominant character of the reaction. That feature comes from the less dissipative collisions involving the $Z_{\max} \sim Z_{\max-1} \sim 17$ component discussed above. On the other hand, the broad bump around the low value of $\text{Asym}_{123} \sim 0.2$ reflects products emitted from a more dissipative midperipheral process as just proposed above for the numerous events pointing at $Z_{\max-1} \sim Z_{\max} \sim 12$ [Figs. 3(d_2) and 3(d_3)]. The distribution extends down to $\text{Asym}_{123} \sim 0$ toward some few events with lighter and lighter fragments approaching the same size. Hence, they appear as issued from strongly excited polysources or from a very elongated excited single source. In contrast, the single-source plot (a_4) behaves in a very different way since it exhibits quite a broad distribution extending from $\text{Asym}_{123} \sim 0.3$ to about 0.85. The main structure peaks around 0.6, while a weaker structure appears at the highest experimental Asym_{123} values (∼0.8), typical of an evaporative process.

It can be summarized that the strong variations, from (a) to (d), of the Z and $Z_{\max}$ distributions, together with the charge correlation between the two heaviest fragments in each event and the evolution of the asymmetry variable Asym_{123}, are strongly suggesting a change in the collision process. These trends are also corroborated by the *mean multiplicities* quoted in Table I, which show a small decrease, from

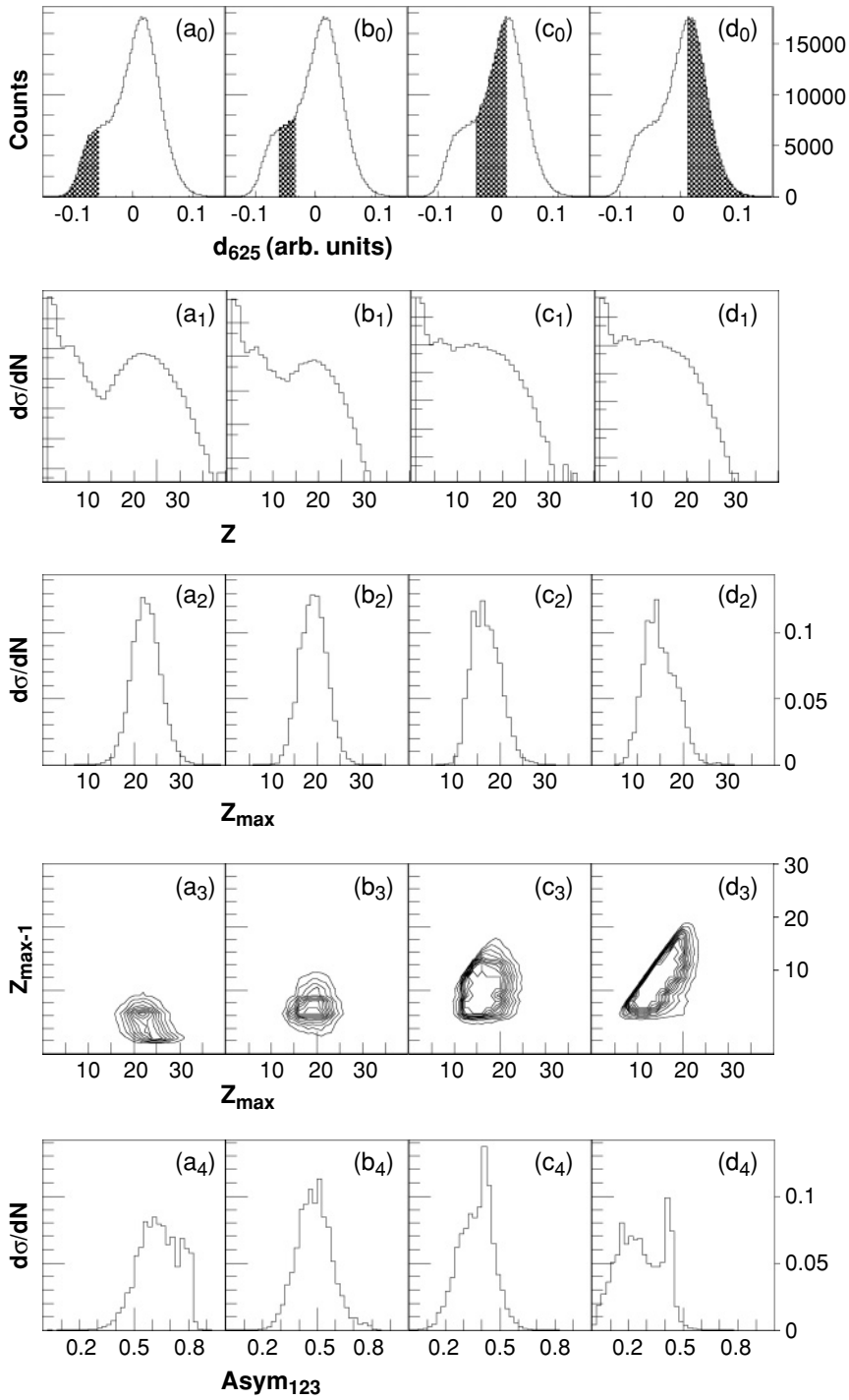

FIG. 3. *Static variable* evolution, according to the four (a_0)–(d_0) intervals (as shown on top row) forming the whole d_{625} distribution. Corresponding plots are displayed for Z charge (a_1)–(d_1), Z_{max} charge in the event (a_2)–(d_2), correlation of the two heaviest fragments (a_3)–(d_3) (axis z with a logarithmic scale), and $Asym_{123}$ (a_4)–(d_4) (see text). Note that the plots were normalized to the number of events [except (a_3)–(d_3)] independently for each plot.

(a) to (d) for low-Z, light charged particles (LCP, defined as $Z < 3$), products which dominate the total multiplicity. This trend, while the multiplicity of fragments is increasing and corroborates the size decrease of the biggest or residuelike partner, also confirms the presence of quite dissipative events in (d). This favors the concept of the fragmentation of the binary projectilelike targetlike subsystem, which is to be related to features mentioned just above for Fig. 3(d_2).

Finally, all these experimental features explain the *a priori* name attribution of the different cuts (a)–(d), and particularly the pure single- and poly source ones for the (a) and (d) samples, respectively. Furthermore, similar global features definitely appear to govern and confirm the so-called whole single-source bumps (a) + (b), on one hand, and, on the other hand, whole polysource (c) + (d) bumps. Note that the representativeness of the events selected in the (a) or (b) regions [respectively, (c) or (d) regions] is not exactly the same as for the selected events in the whole single [poly] source bump. For example, events of the (a) region contain more asymmetric partitions than events of the (b) region.

TABLE I. Mean (total, LCPs, and fragments) multiplicities, mean total charge of the fragments, and mean total charge of the events, according to the four intervals delimited by the d_{625} discriminant variable (see text).

d_{625} interval	Single (a)	Single+poly (b)	Poly+single (c)	Poly (d)
Total multiplicity	17.5	17.0	16.3	15.1
$Z = 1$ multiplicity	9.7	8.8	8.3	7.2
$Z = 2$ multiplicity	5.6	5.5	5.2	4.8
Fragment multiplicity	2.6	3.1	3.3	3.6
$\langle Z_{\rm tot}\rangle$fragments	28.3	29.2	31.0	32.8
$\langle Z_{\rm tot}\rangle$	49.5	49.2	49.7	49.6

The characterization of the evolution of the mechanisms as clearly observed above (from single-source fusionlike characteristics to a binarylike source scenario) will be studied in more detail in the following section.

2. *Kinetic and shape variables*

The diagrams of Fig. 4 are devoted to the study of shape and kinetic variables gated by the d_{625} cuts as defined for Fig. 3. The variables are defined in the experimental center of mass (c.m.) of the event. Since we deal only with complete events, the measured velocity in the laboratory (average $V_{\rm c.m.} = 4.02$ cm/ns) is always very close to the one calculated from the initial kinematics, i.e., $V_{\rm c.m.} = 3.93$ cm/ns. These plots represent (from top to bottom) coplanarity versus sphericity, charge versus parallel (to the beam axis) velocity, perpendicular (to the beam axis) versus parallel velocity, and mean fragment kinetic energies $\langle E_{\rm kin}\rangle$ versus their charge Z.

The first row displays the coplanarity C versus sphericity S plots. Such global variables are related to the event shape. These plots indicate that the single-source events selected by the d_{625} criterion [Fig. 4(a_5)] show spherical shapes ($S \sim 0.7$). This indicates a more isotropic single-source emission than for the opposite in case (d_5), where the binarylike selected events appear more concentrated close to the elongated shape corner ($S \sim 0.4$).

In the second row, the behavior of the charge versus parallel velocity $V_{\rm par}$ reveals from (a_6) to (d_6) a spectacular change in the mechanism. Indeed, in Fig. 4(a_6), the picture exhibits a single-source emission pattern globally centered on the c.m. However, a fraction of the light ($Z \leqslant 8$) fragments appear a bit more concentrated forward of the c.m., while the heavier fragments ($Z \geqslant 15$) lie at a velocity slightly negative. This effect is due to detection thresholds. Indeed the plot includes two main components, a high-Z component ($15 \leqslant Z \leqslant 30$) well defined in both Z and $V_{\rm par} \sim 0$, and a widely spread $V_{\rm par}$ component corresponding to light fragments ($Z \leqslant 8$) and numerous LCPs. There is a depletion of fragments with $Z \sim 8$–15 between these two components, as already observed in Fig. 3(a_1). A continuous evolution is visible through the three other plots, up to (d_6) reflecting a binarylike distribution. The two peaks pointing symmetrically from each side of the velocity $V \sim 0$, at ± 3 cm/ns, correspond to the projectilelike and targetlike contributions. Both peaks contain charge with Z ranging mainly from ~13 to ~25.

The evolution of the processes is also evidenced through the invariant contour plots, $V_{\rm per}$ (velocity perpendicular to the beam) versus $V_{\rm par}$ (3rd row), undeniably reflecting the gradual transition from a single-source pattern to a better and better separated bisource pattern related to the binarylike character of the projectile and the target components.

Finally, the correlation of particular interest (bottom of Fig. 4) between the mean kinetic energies and the charges of the fragments ($Z \geqslant 3$) also reveals completely different underlying mechanisms according to these d_{625} intervals. More precisely, the two lines (a_8)–(d_8) and (a_9)–(d_9) concern, respectively, events without and with a cut on events inside a cone with $\cos\theta = \pm 0.5$ (in the measured center of mass). In addition, empty squares and dark triangles symbolize events with and without the heaviest fragment, respectively.

As it can be seen in Fig. 4(a_8), for the heaviest fragment ($Z \sim 14$–32), the mean kinetic energy remains low and is slightly decreasing (from ~30 to ~20 MeV). This behavior is then assimilated to an evaporation residue pattern, compatible with an incomplete fusion scenario followed by a sequential evaporation process. It is interesting to stress this particular energy slope breakdown (from ~70 to ~30 MeV) between $Z \sim 10$ and ~14, where the charge yields are the lowest as observed in Figs. 4(a_6) and 3(a_1). This point will be discussed in Sec. V.

The pure polysource events (d_8) exhibit a strong increase, from ~40 to ~180 MeV. Increasing kinetic energy with charge can obviously be attributed to a dominant binary character of the collision, keeping memory of the entrance channel, specially for the heaviest ($Z \geqslant 16$) products. These fragments are related to the less dissipative component of the binary mechanism.

For comparison, we now consider the same curves (a_8)–(d_8) but with the heaviest fragment of the event removed (dark triangles). These curves clearly enhance the completely different behavior of the pure single-source events with respect to the others. When the heaviest fragment is removed, no fragment with charge over 14 is observed in the pure single-source events [events that correspond to very low statistics were suppressed in Fig. 4(a_8)–(d_8) and (a_9)–(d_9)], whereas fragments with charge up to 20 are still observed in the pure polysource events. This shows that in pure single-source events a quite heavy residue can be still observed, whereas most pure polysource events contain two heavy fragments.

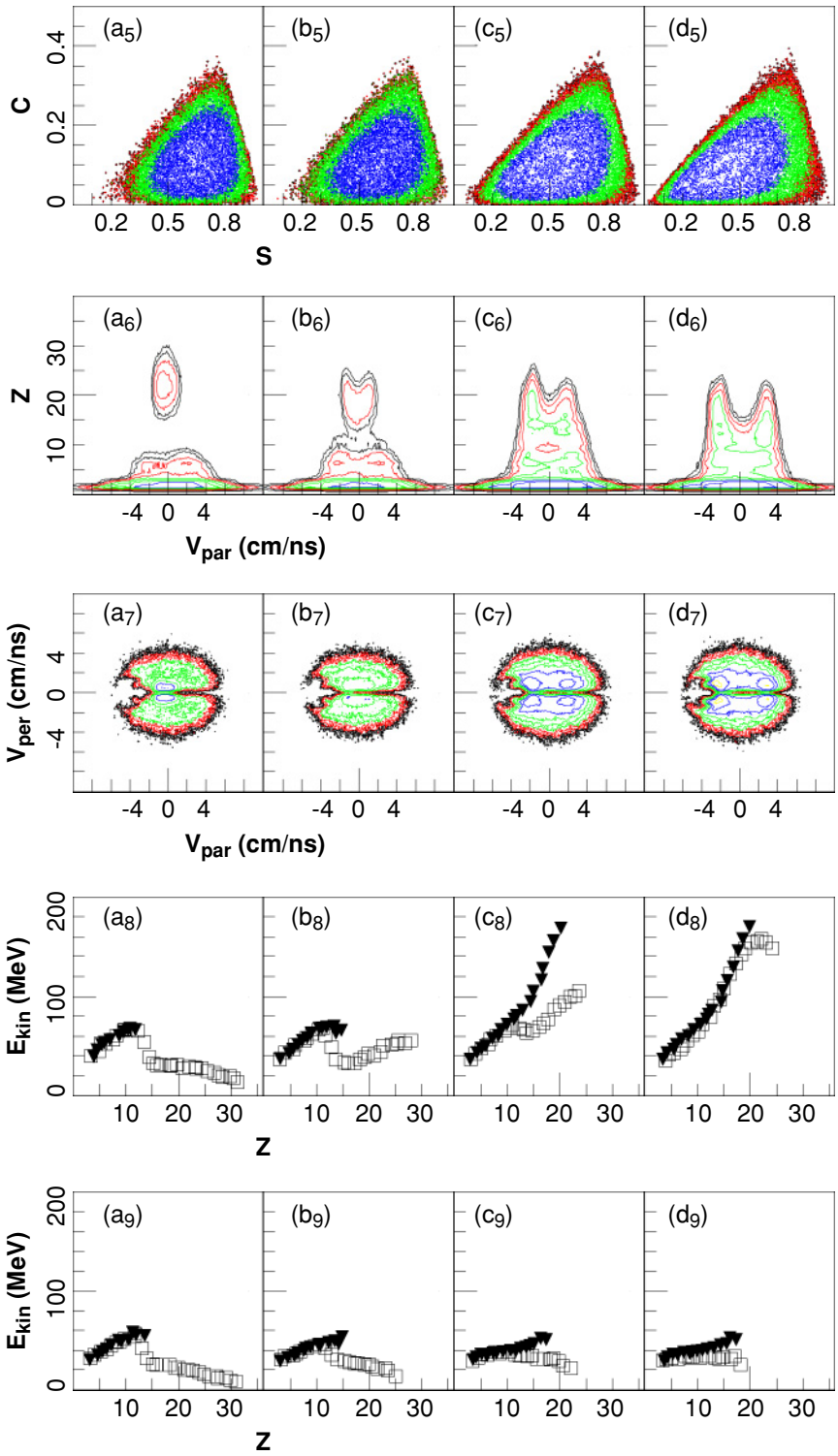

FIG. 4. (Color online) *Kinetic variables* evolution, according to the same d_{625} intervals as in Fig. 3. Coplanarity versus sphericity (a_5)–(d_5); charge Z versus parallel velocity (a_6)–(d_6) (for the first three rows, axis z corresponds to a logarithmic scale); V_{per} versus V_{par} (a_7)–(d_7); mean kinetic energy E_{kin} of each fragment *with* (open squares) and *without* (black triangles) the Z_{max} of the event (a_8)–(d_8). The last row stands for the same E_{kin} as above but with a cut on the forward/backward angular region (see text).

Coming back now to these numerous lighter fragments with $Z \sim 3$–10, we note that their mean E_{kin} steadily increase from ~40 to ~70 MeV. Moreover, this behavior seems to keep the same increase $\langle E_{kin} \rangle$ with the charge whatever the d_{625} interval, (a_8)–(d_8), i.e., whatever single(poly) source is involved, hence over a rather large impact parameter range; this behavior is worth noting. This trend was already observed in the heavier Xe+Sn system at 50 MeV/nucleon [19].

As a check on the reliability of the data, the angular cut (as defined above) performed in the pure binary case of Figs. 4(d_8) and 4(d_9) exhibits on the opposite end a spectacular change. Indeed, the strongly increasing $E_{c.m.}$ from 40 ($Z = 3$) to 160 MeV ($Z \sim 23$) (empty squares and full triangles standing for with and without Z_{max}, respectively) is suppressed by the angular cut, as expected from such binary collisions with a strong memory of the entrance channel. Indeed it is replaced

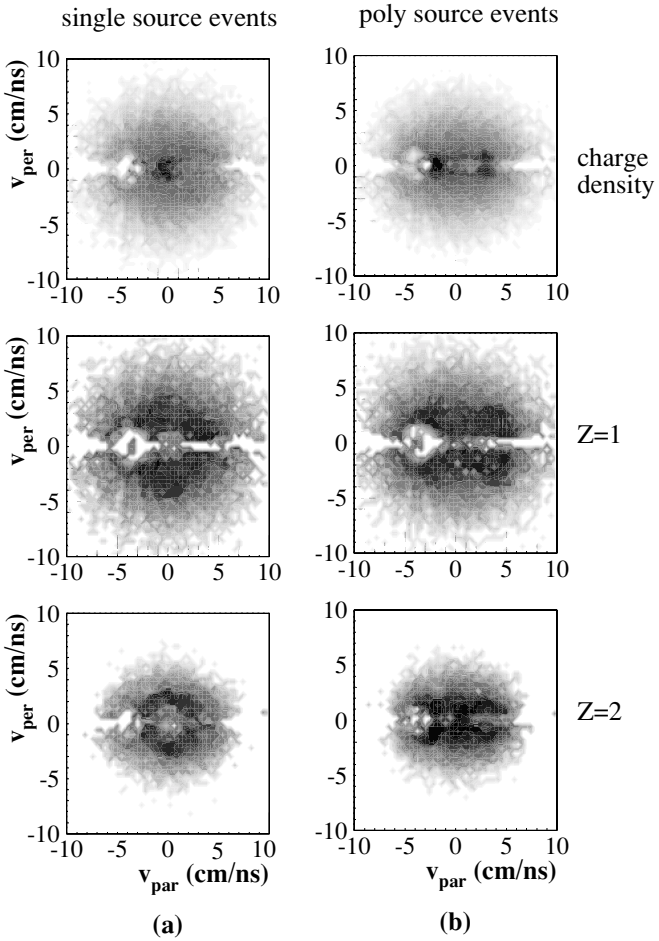

FIG. 5. *Velocity diagrams* $V_{\rm per}$ versus $V_{\rm par}$ for (a) single-source events and (b) polysource events in three cases: each fragment weighted by its charge, $Z=1$, $Z=2$ (rows 1, 2, and 3, respectively, axis z with a logarithmic scale).

[in (d_9)], and for both symbols, by a wide plateau extending from $Z=3$ to $\sim$20 with constant $\langle E_{\rm c.m.}\rangle > \sim$30 MeV. Such a behavior reflects the presence of some transverse energy contribution due to the most dissipative collisions in (d), as previously observed, for example, in the heavier Xe+Sn system at 50 MeV/nucleon [19]. These features are also confirmed in the data obtained with such an angular cut performed on the $Z_{\rm max}$ plot, where the very less dissipative binary component [above $Z_{\rm max} \sim$ 17 in Figs. 3(d_2) and 3(d_3)] is found to disappear, thus leading to an enhancement of the most dissipative one around $Z_{\rm max}=12$ (and even, to a lesser extent, around $Z_{\rm max}=8$).

The diagrams of Fig. 5 show in more detail the single and polysource patterns for $Z=1$ and 2 particles and for the *charge density* (i.e., velocity diagram weighted by the Z charge of all products). These patterns are confirmed both for $Z=1$ and 2 particles, while the charge density diagrams emphasize these trends for all fragments and particles. One can remark, however, that the polysource pattern exhibits a "midrapidity" emission, especially for the $Z=2$ case. This contribution disappears in the fragment case (i.e., the fragment density at midrapidity is lower than 1/30 of its maximum).

It might be noted that all this topology was already visible in the raw data of Fig. 2 when comparing the proposed pure single-source and pure polysource labels. Furthermore, we have checked that more restrictive cuts, for the pure single-source sample events, do not affect the characteristics of the events presented in Figs. 3 and 4. Hence, the partition probabilities are unchanged whatever the cut applied in the first half of the first Gaussian function which corresponds to pure single-source events. Only the number of events is affected by the cut. As the aim of this work is to sort out pure single-source sample events, it is obvious that a less restrictive cut would not be appropriate. To summarize, this overview of experimental observables demonstrates the efficiency of the DA method and its related d_{625} variable to clearly disentangle a major presence of single-source events related to the lowest values of this variable from the dominant bisource events related to its highest values.

We now have to further characterize the selected pure single-source events that present strong features of a fusionlike process, suggesting from the above experimental study the formation of a highly excited subsystem. Indeed, quite a large energy dissipation can be observed from these 32 MeV/nucleon Ni+Ni collisions, whatever the involved subsystem, relevant to a single- or polysource pattern. The hypothesis of a hot compound system will be discussed in the next section, in which the analysis is focused on the pure subset of single-source events.

IV. SINGLE-SOURCE CHARACTERIZATION

Thanks to the d_{625} description of our data, we managed to sort out pure single-source events, giving strong support to a well-defined emitter. As mentioned in Sec. III B, the very clean selection favors more asymmetric partitions in the exit channel. The nature of this source will be determined with more precision, particularly via a study of emission processes leading to the final products.

A. Equilibrium and preequilibrium emission

A simple way to look for *thermal equilibrium*, as involved, for example, in the evaporative process of a hot source, is as just mentioned above, is by studying the Maxwellian and isotropic behavior of the particle energy spectra.

Afterward we shall examine more quantitatively the deviations from such a supposed isotropic particle emission, which could be due to preequilibrium effects. For that purpose the total experimental angular region has been divided into eight domains as determined in [3], in the c.m., in order to cover equivalent solid angle sectors.

In a first step, taking into account that the nonequilibrium effects are mostly expected at forward/backward angles (symmetric systems), this anisotropic component will be excluded from the angular distributions by suppressing particles emitted outside a cone between $\theta_{\rm c.m.}=60^\circ$ and 120°. Then the related four sectors cover the intermediate angular range, i.e., part

TABLE II. Equilibrated emission (part B): particle mean kinetic energies compared to the expected values from a classical statistical emission and "apparent" temperatures from Maxwellian fits ("Surf" for surface; "Vol" for volume).

Particle	p	d	t	^{3}He	α	$3 \leqslant Z \leqslant 8$	Z_{max} only	All fragments
$\langle E_{exp} \rangle$ (MeV)	18	20.5	21	23.5	21	37	19	30
$\langle E_{simon} \rangle$ (MeV)	19	23	22.5	25	24	—	—	—
T_{exp}^{app}(MeV) Surf(Vol)	9(11)	10(11)	10.5(12)	11.5(12)	10(12)	18.5(18)	11(12.6)	19(18)

B (Figs. 6 and 7), whereas part A is concerned with the four extreme backward and forward angular sectors. Energy distribution spectra from part B are displayed in Fig. 6 for the various LCPs and fragments. In these conditions one observes quite similar slopes for protons, deuterons, tritons, and α's (see Table II) as expected from equilibrated emission (note that the slope for Z_{max} is close to the one for light particles). This feature is reinforced in Fig. 7 where, in part B, the four energy distribution sectors for $Z = 1$ (left column) and $Z = 2$ (right column) particles are put together. They appear quite superimposable, opposite to part A which includes the four extreme backward and forward angular sectors. Indeed, these similar slopes in B reflect (Fig. 6) a same apparent mean "temperature" as quoted in Table II, i.e., around $T \sim 10$–11 MeV for LCPs (surface or volume emission formulations lead to comparable temperature results, though fits are better for the low energies $\leqslant$20 MeV with a surface emission, while a volume one better accounts for the higher energies). We remark at this stage that these temperature parameters appear relatively high for a pure sequential decay scenario, while the light fragments involve a much higher T_{app} as reported in Table II.

However, the mean kinetic energies of the concerned species reported in Table II are compatible with expected values from a statistical emission calculation as performed by the SIMON code used in its standard statistical sequential decay approach. One may notice (Table II) no significant deviation for the ^{3}He-particle mean kinetic energy from the other experimental light-particle values. However, they exhibit a rather different shape at the beginning of their energy spectra where the small energy component is suppressed, compared to the other particle spectra. Such ^{3}He specificity has previously been pointed out in INDRA data [21], where this effect was found to be much more pronounced through a study of a heavier and more energetic system and was attributed to an early ^{3}He emission from the hot compressed compound nucleus.

Regarding the slopes of each class of particles, a hierarchy is observed in the emission of the different products. Light fragments appear to be issued from a more excited system than α's

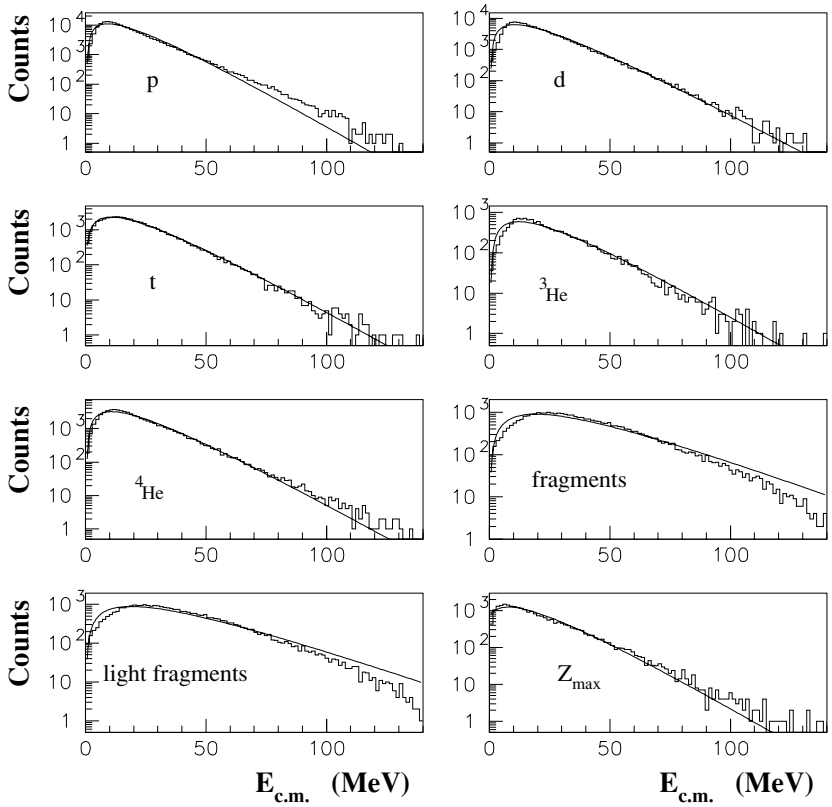

FIG. 6. Center-of-mass energy distributions (histograms) for $60^\circ \leqslant \theta_{c.m.} \leqslant 120^\circ$ (part B), for protons ($\chi^2 = 5381.0$), deuterons ($\chi^2 = 6830.0$), tritons ($\chi^2 = 228.7$), ^{3}He ($\chi^2 = 643.0$), ^{4}He ($\chi^2 = 1175.0$), fragments ($\chi^2 = 1769.0$), light fragments ($3 < Z < 8$, $\chi^2 = 1737.0$), and Z_{max} ($\chi^2 = 654.4$). The continuous lines stand for Maxwellian adjusted distributions (surface emission type).

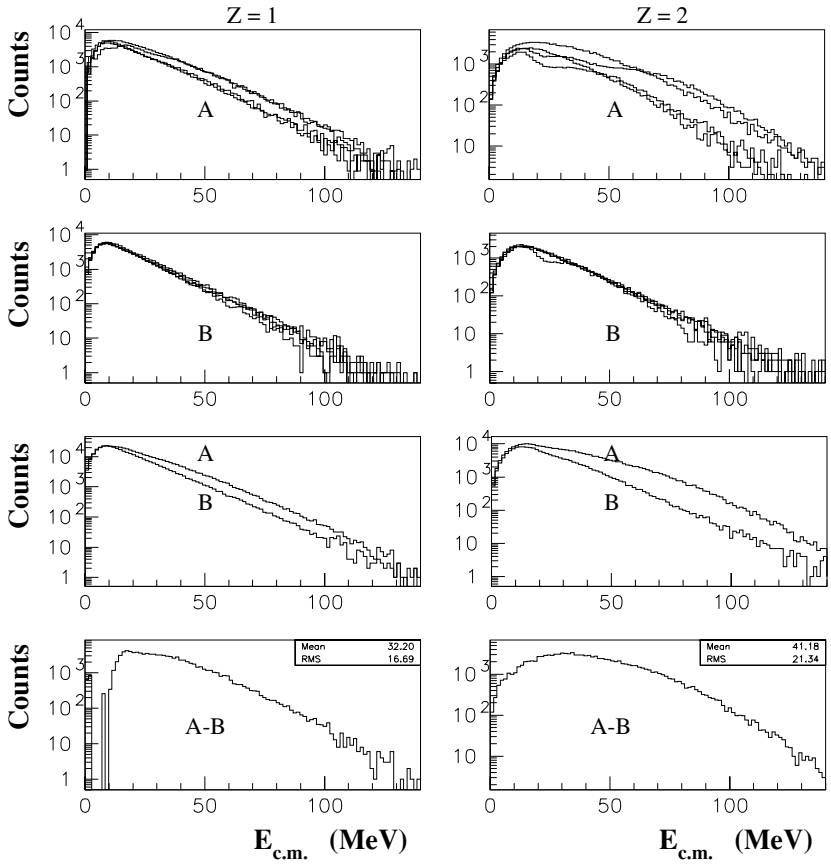

FIG. 7. Center of mass $Z = 1$ (left column) and $Z = 2$ (right column) energy spectra for various angular domains (see text): row 1, part A extreme angular sectors ($\langle 29^\circ \rangle$, $\langle 50^\circ \rangle$, and $\langle 129^\circ \rangle$, $\langle 151^\circ \rangle$); row 2, part B intermediate angular sectors ($\langle 68^\circ \rangle$, $\langle 83^\circ \rangle$, $\langle 97^\circ \rangle$, $\langle 112^\circ \rangle$); note that the irregularity induced by the detector, observed for $Z = 2$ at backward angles, does not affect the difference (A − B) in the last row; row 3, A and B summed angular sectors; row 4, center-of-mass subtracted energy spectra for emitted preequilibrium.

and protons, as expected from statistical emissions involving sequential decays as well as prompt multifragmentation.

In a second step, to better define the emitter, we need more quantitative information about the above-mentioned *preequilibrium* stage of the reaction. For that purpose, we consider in Fig. 7 the energy spectra of $Z = 1$, 2 products emitted in parts A and B described above. The particle emission in part A, which involves the four most backward/forward regions, appears clearly to deviate, mainly at extreme forward/backward angles, from isotropy. Obviously, part A appears to include a preequilibrium contribution. Therefore, subtracting the thermal component observed in part B from part A leads to a reasonably good estimate of the preequilibrium energy spectra. The $Z = 1$ preequilibrium energy spectrum reveals (Fig. 7, bottom) a dissymetric component of energetic particles pointing around $E_{\mathrm{c.m.}} \sim 18$ MeV but with a mean value at $\langle E_{\mathrm{c.m.}} \rangle \sim 32$ MeV. Among these $Z = 1$, the proton emission, which is dominant (∼55%), would then correspond to a mean velocity of ∼7.5 cm/ns, i.e., ∼2 $V_{\mathrm{c.m.}}$ (3.93 cm/ns). We have observed that the total $E_{\mathrm{c.m.}}$ mean values for deuterons and tritons are roughly the same as for protons, i.e., around 30 MeV. The same procedure applied to the $Z = 2$ preequilibrium emission particles leads to a broader and more symmetrical distribution, centered around $\langle E_{\mathrm{cm}} \rangle \sim 40$ MeV, corresponding to ∼4.3 cm/ns for dominant α particles, i.e., $\sim 1.1 V_{\mathrm{c.m.}}$.

These differences between preequilibrium protons and alphas imply that their emission dynamics are not the same. We may suggest, as shown in [22], that such energetic protons extending up to ∼110 MeV (the kinematical limit being ∼80 MeV) are mostly emitted through *N-N* collisions in the first stage of the reaction [23]. Similar interpretation of the α emission is not so obvious and could be related to this peculiar process previously observed in central collisions, i.e., the so-called spray effect [5,7], responsible for α and light-fragment forward emission in a fusionlike process. Indeed, it has been shown for ^{40}Ar+Cu, Ag, Au for 17–115 MeV/nucleon incident energy that the initial composite system mass also decreases with energy, but by a relatively small amount. These central collisions can be said to change gradually from incomplete fusion with capture of most of the projectile to "splintering" central collisions with capture of only a small fraction of the projectile nucleons. The early reaction dynamics generate a multibody spray of nucleons and fragments ejected in the forward direction (i.e., that of the Ar projectile). In the present work, some light fragments (from $Z = 3$ to ∼8) are also observed, at $\langle E_{\mathrm{c.m.}} \rangle \sim 59$ MeV, but with such low statistics that this last emission is neglected in the following analysis. Hence, if it exists, such a spray effect (in which the nucleons and fragments should be ejected in the forward and backward directions in a symmetric system) will not be taken into account in this Ni+Ni medium-size system at 32 MeV/nucleon incident energy.

As we need to obtain an event-by-event estimate of a global charged preequilibrium emission, we have attempted different procedures to deduce these experimental quantities.

TABLE III. Preequilibrium emission (part A): mean numbers of total emitted charges and neutrons. Predictions and experiment.

	Charges $Z = 1$	Neutrons
SIMON code	6 ± 1	6 ± 1
BLANN code	6 ± 1	10 ± 2
BNV code	4 ± 2	4 ± 2
Experiment	7 ± 1	9 ± 2

First we considered the subtraction A − B for each species (see Fig. 7) relative to its total yield A + B (i.e., $\leqslant$20% for $Z = 1$ and ∼30% for $Z = 2$). Another method used the integrated Maxwellian fitted curves. A third one was based on the shape of the angular distributions. Last, we followed the prescription of [24]. It is thus important and comforting to stress that whatever the method, all the deduced estimations for charged preequilibrium components converge toward similar values such as

$$Z_{\text{preeq}} \sim 7 \text{ charges},$$

with a charge multiplicity dispatched as

$$M_{Z=1} = 3 \qquad \text{and} \qquad M_{Z=2} = 2.$$

These values were corrected for the detector bias. Finally, this estimation will help us to determine the size and excitation energy of the source, as presented in the next paragraph.

B. Size and excitation energy of the single source

Now we have to add the neutron contribution to the experimentally deduced total Z_{preeq} emitted *charge* to first extract the total amount of nonequilibrated emitted matter and then evaluate the *size* of the source. The number of preequilibrium neutrons can be evaluated using two different prescriptions. On one hand, it is reasonable to suppose that the isospin equilibration is realized at the first instant of the reaction by ejecting the four exceeding neutrons accompanied by light charged cluster (*d*, *t*, He) emissions. On the other hand, the *N*/*Z* ratio can be considered as remaining the same in the preequilibrium component as in the entrance channel. Both assumptions lead to compatible values which can be estimated at about 9 ± 2 neutrons. The minimum amount of preequilibrium emitted *mass* is then deduced as

$$A_{\text{preeq}} \sim 16 \text{ mass units},$$

thus leading to the size of the source

$$A_{\text{source}} \sim 100,$$

since $A_{\text{tot}} = 116$ and $Z_{\text{tot}} = 56$, with $Z_{\text{source}} \sim 49$.

Table III displays the results of this estimate, together with the estimates for protons and neutrons given by various predictions using the SIMON, BLANN [25], and BNV [26] models. We recall that in such models, the preequilibrium calculation is performed only for nucleons. Therefore, the comparison makes sense only for the total emitted charge. Both the SIMON and the BLANN codes provide a quite quantitative agreement with the data.

The excitation energy stored by the single source has been evaluated by a calorimetric method [27], after subtraction of the preequilibrium component estimated just above. This method takes into account the Q value of the reaction, the kinetic energies of detected products, an estimated energy for the neutrons, and a residual excitation energy of the hot nucleus. As a result, a mean value of $\langle E^* \rangle \sim 500$ MeV or ∼5 (±0.8) MeV/nucleon is obtained for a total mass number of the emitter $A_{\text{source}} \sim 100$. Since the total available energy in the Ni+Ni system at 32 MeV/nucleon amounts to 835 MeV in the c.m., i.e., ∼7.2 MeV/nucleon, this leaves $E_{\text{preeq}} \sim 335$ MeV for the energy carried out by the preequilibrium emission. According to our deduced preequilibrium yields and related mean kinetic energies (Fig. 7), we then obtain values compatible with the one deduced just above. This measured excitation energy per nucleon of the fusionlike nucleus is relatively high and, moreover, close to the multifragmentation threshold defined as the passage from dominant two-body to multibody splitting of hot heavy nuclei [8]. We emphasize that our data could then extend such a description to medium-size symmetric systems.

In summary, it appears that most of the incident mass (∼86%) and only about half of the initially available energy (∼55%) of the system are devoted to the formation of a relatively hot and equilibrated subsystem. Hence, it is the early emission of prompt light particles that permits the formation of the excited composite nucleus. We now examine its decay modes.

V. CHARACTERISTICS OF THE DECAY CHANNELS

A fundamental question raised in the phenomenology of multiple fragment production lies in its sequential evaporation or simultaneous multifragmentation character. The latter sets a link with the equation of state, whereas the sequential case refers to an extension of the standard and dominant evaporative decay mode, as observed for a long time at lower incident energies ($\leqslant$20 MeV/nucleon, where a heavy residue is accompanied by LCPs).

A. Sequential decay

A strong indication of such a fusionlike sequential evaporation process can be seen in Fig. 8, which displays the two-dimensional plots of the charge Z of each fragment as a function of its velocity expressed in the c.m. frame. Plot (a) shows the same correlation as in Fig. 4(a_6) but includes only fragments; plot (b) illustrates the case where the heaviest fragment Z_{max} of each event has been excluded: we clearly observe only the remaining low-charge fragments ($Z \leqslant 12$) with velocities spread between $\sim \pm 4$ cm/ns (i.e., $\pm V_{\text{proj}}$). Moreover, the study of these selected events shows that they all systematically include one relatively heavy fragment around the c.m. velocity. The mean charge of the heavy fragment stands around $\langle Z_{\text{max}} \rangle = 22$ ranging from ∼12 to ∼35 [Fig. 3(a_2)]. Moreover, in this high $\langle Z_{\text{max}} \rangle$ value region, the mean kinetic energy $\langle E_{\text{c.m.}} \rangle$ of the fragments [see Fig. 4(a_8)] is

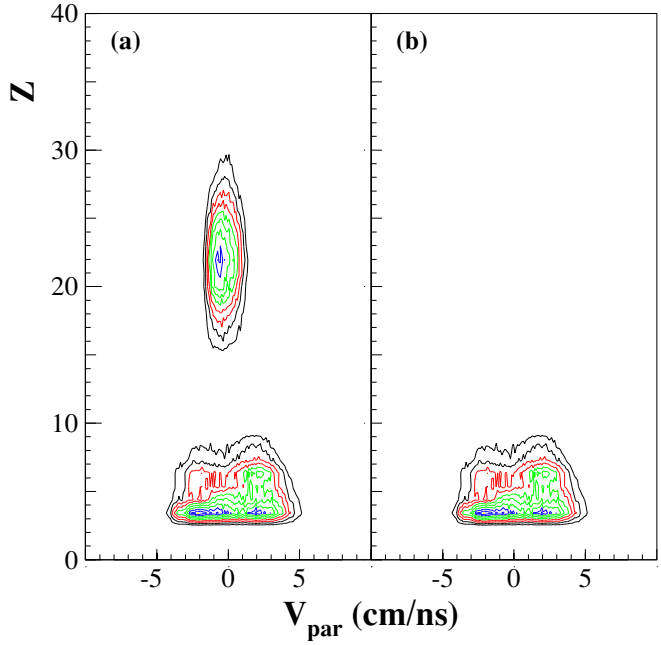

FIG. 8. (Color online) Charge velocity diagram (a) with and (b) without the heaviest fragment; for both plots, axis z corresponds to a logarithmic scale.

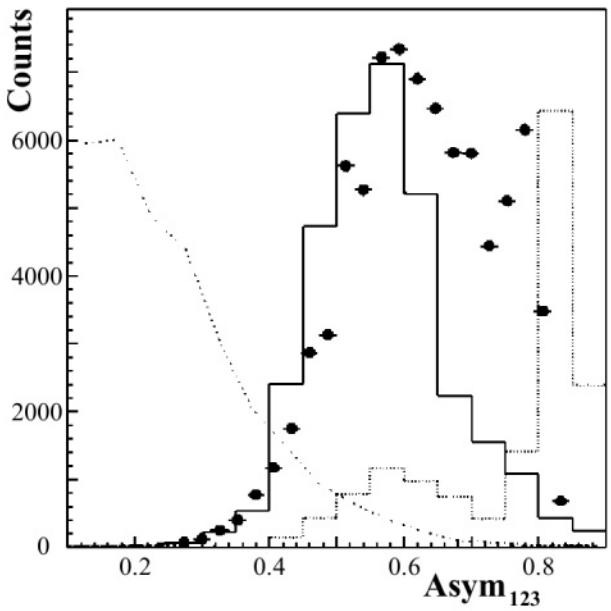

FIG. 9. Charge asymmetry (Asym_{123}): black dots stand for the data. The model distributions SMM (full line histogram), GEMINI (dotted line histogram) and random mass partitions (dashed-dotted line) (see text).

low and slowly decreasing with $\langle Z_{\max}\rangle$ increasing. Thus, this feature *a priori* would support a standard evaporation scenario, leaving a relatively heavy residue, with numerous LCPs and some intermediate mass fragments (IMFs), which are defined as fragments excluding the heaviest product. However, note that this $\langle Z_{\max}\rangle$ value would correspond to a rather low-size residuelike value as compared to $Z_{\mathrm{source}} \sim 50$ and to a total fragment emitted charge $\langle Z_{\mathrm{tot}}\rangle \sim 28$. This is all the more true for the events in which the heaviest fragment has a charge as light as 15.

We now turn back to the charge asymmetry Asym_{123} distributions of Fig. 9. This figure compares the data [already displayed in Fig. 3(a_4)] with some models. The slight peaking at the highest values, i.e., ~0.8, was already pointed out as characterizing a pure sequential decay component. Indeed, this relatively weak structure corresponds to the highest values of $Z_{\max}$ accompanied by the very lowest $Z_{\max\text{-}1}$ values ($Z \leqslant 3$), corresponding to the lowest islet in Fig. 3(a_3). However, it constitutes only a small part of the whole Asym_{123} distribution, the remaining dominant part being spread around 0.6 and related to events that include a relatively light $Z_{\max}$ accompanied by fragments (mostly with $Z \sim 4$–8) and LCPs. With nothing being left at $\mathrm{Asym}_{123} \leqslant 0.3$, we do not observe nearly equal size events as we might have expected in the framework of a spinodal process [28].

Finally we have shown that the decaying process for the Ni+Ni system at 32 MeV/nucleon presents, at least for a significant part of the sample, some typical characteristics of an evaporative scheme. This is clearly evidenced in Fig. 8 and for the events belonging to the relatively small and narrow peak at the largest asymmetry ($\mathrm{Asym}_{123} \sim 0.8$) values (Fig. 9). This structure corresponds to events involving mostly a residue of size $25 < Z < 35$ and LCPs and represents about 10% of the single-source events. They indeed may be considered as pure sequential evaporative decays.

The GEMINI [29] code, which describes the single-source emission within the framework of sequential decay, has been used with input parameters equal to the values deduced above for the single-source size ($Z = 50$, $A = 100$) and excitation energy ($E^* = 5$ MeV/nucleon). It indeed reproduces, as shown in Fig. 9, large asymmetries (dotted line) with a strong dominating peak at $\mathrm{Asym}_{123} \sim 0.8$, but fails to describe the major part of the experimental distribution centered around $\mathrm{Asym}_{123} \sim 0.6$. This inconsistency was observed throughout a backtracing procedure (detailed in [2,30]) performed with the GEMINI model. The confrontation with experimental static (Z charge, $Z_{\max}$, etc.) and kinetic (charge Z versus V_{par}, V_{per} versus V_{par}, etc.) variables has shown that at high excitation energy [2], this model overestimates the production of light particles. This explains the small shift between our experimental peak and the GEMINI peak. Hence, we confirm the sequential evaporation character of a part of the single-source decays with a charge partition Asym_{123} around 0.8.

Furthermore, to check these data against a possible trivial peaking, the so-called dynamic minimum hypothesis (DMH, Monte Carlo calculations) has been developed [31]. The input parameters of this toy model are the total charge and the excitation energy (here $Z_{\mathrm{tot}} = 50$ and $E^* = 5$ MeV/nucleon). The charge partitions are generated through the hypothesis that all possible partitions from Z_{tot} compatible with the available energy have the same probability (minimum information model). Energy and momentum are conserved event by event.

These DMH events are filtered in order to account for the detector biases. We observe that the experimental splittings

depart clearly from this minimum-biased simulation (dashed-dotted histogram, Fig. 9). This confrontation shows that the structure at $\mathrm{Asym}_{123} \sim 0.6$ cannot be accounted for by some fortuitous filtering or combinatory effects in the mass partitions. Therefore, an alternative process, departing from the classical sequential evaporation picture, has to be invoked in order to, for example, satisfactorily reproduce the observed overall asymmetry distribution. The correlative question is to identify the multiple fragment deexcitation mechanism corresponding to this dominant remaining part of the data sample.

B. Multifragmentation from phase coexistence?

To hunt for this deexcitation mechanism, the experimental sample is analyzed with a statistical multifragmentation model (SMM) [32]. SMM has been used with the same input parameters as for GEMINI, and the same criteria as for the experimental data have been applied. The results for the Asym_{123} distribution are shown in Fig. 9 (full line). The dominant stucture at $\mathrm{Asym}_{123} \sim 0.6$ can be rather well reproduced, whereas the high asymmetry part and the narrower structure at $\mathrm{Asym}_{123} \sim 0.8$ are not accounted for. This latter structure is reproduced by the GEMINI distribution but with a rate much greater than in the experimental distribution. Taking into account the relative intensity of the two structures observed in Fig. 9, we tried to mix the two processes. Hence, a backtracing procedure in which GEMINI and SMM are free parameter was performed. Some 90% of SMM events and 10% of GEMINI events are found, which satisfactorily reproduce experimental static (Z charge, Z_{max}, etc.) and kinetic (Z charge versus V_{par}, V_{per} versus V_{par}, etc.) variables [2]. Note that a less restrictive cut in the d_{625} distribution to select single-source events affects the relative intensity between the two structures (but cannot filled up the intermediate minimum) in the Asym_{123} distribution with an increasing number of events with $\mathrm{Asym}_{123} \leqslant 0.7$ [see Figs. 3(a_4) and 3(b_4)]. Thus, the 90% (10%) of SMM (GEMINI) events appears to be a minimum (maximum) proportion.

This duality in the data between evaporative and simultaneous multifragment emission agrees with previous analyses [1,8] which locate the onset of simultaneous multifragmentation around 30 MeV/nucleon incident energy. Moreover, a significant amount of collective motion has been shown to appear [1] beyond a beam energy of about 30 MeV/nucleon for heavier central symmetric collisions at excitation energies greater than about 5 MeV/nucleon. This is to be related to the suggestion [8] that the transition from sequential to simultaneous fragmentation, i.e., from decay at normal density to disassembly at a lower density, is expected to be coupled with the onset of matter expansion. At this stage we stress that the analysis of mean kinetic energies constitutes an experimental signature for radial autosimilar collective motion. We observe in Fig. 4(a_8) that the light fragment energy increases with its charge. This effect, difficult to explain in an evaporative scenario (see above), clearly recalls the behavior of the lighter fragments in symmetric heavier systems such as Xe+Sn [3,19,33] and Gd+U [9] around 32 and 50 MeV/nucleon incident energy. The latter systems demonstrated that a small

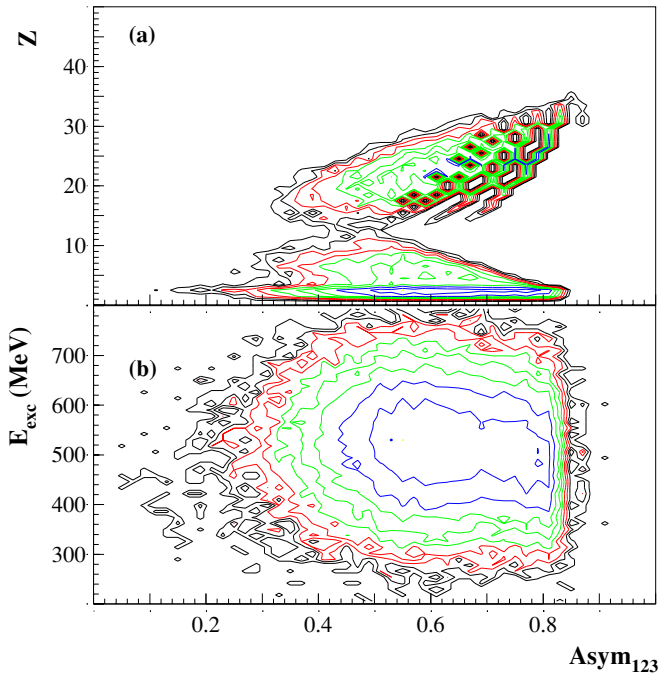

FIG. 10. (Color online) Asymmetry versus (a) charges Z of the fragments/particles of each event, or the so-called butterfly plot, and (b) measured available excitation energy E_{exc} of the composite subsystem; for both plots, axis z corresponds to a logarithmic scale.

radial expansion energy was required, from 0.5 to around 1 MeV/nucleon at ~30 MeV/nucleon incident energy to around 2 MeV/nucleon at 50 MeV/nucleon incident energy. In our case, the result obtained with the SMM model is compatible with no radial expansion energy to explain the distribution in Fig. 4(a_8). However, a small expansion component is hardly measurable, as discussed in the case of heavier systems [9,33].

Therefore, that interesting double aspect (sequential decay and *thermal* prompt multifragmentation) is presently clearly evidenced for the first time for such medium-size symmetric system as Ni+Ni at 32 MeV/nucleon incident energy; it has also been shown recently for a heavier system, Ni+Au, at 32 MeV/nucleon [34]. This duality is also reflected in Fig. 10(a). In this "butterfly" shape, each charge is correlated to its Asym_{123} value. The highest Asym_{123} values essentially correspond, in a narrow domain, to the largest residuelike size, accompanied by LCPs. In contrast, the dominant remaining part is widely spread, progressively extending with decreasing Asym_{123}, toward more fragments but with a depletion (already mentioned above) around $Z = 10$, which progressively fills in.

This duality could hold in the framework of a threshold effect: the onset of a new mechanism (instantaneous multifragment emission) in place of the vanishing evaporative one. However, in this scenario, one might expect a dependence upon the convertible energy; an instantaneous multifragment process should correspond to higher excitation energies than a sequential process. This difference should be visible in the data. To check this effect, we plotted [Fig. 10(b)] the measured available excitation energy in the composite system versus the Asym_{123}. The plot presents a very interesting feature: the two regions of events corresponding to the two different

asymmetry domains discussed above appear at almost the same excitation energy (∼500 MeV). The fact that we see no pronounced correlation between the charge asymmetry pattern and the excitation energy implies that for the selected sample, the charge partition is not governed by this amount of available excitation energy. Indeed, such a two-component decay process cannot be so simply related to the fluctuations of the amount of energy relaxed by preequilibrium emission. We emphasize that for such a hot subsystem various channels are open. Then, a high excitation energy might not necessarily be the signature of a prompt multifragmentation alone, but could be compatible with the coexistence of both decay processes driven by *thermal* fluctuations.

Therefore, the remaining question is to know if the duality in the experimental results is related to a phase transition signal. This framework [35,36] gives an understanding of coexistence as a bimodality of the event distribution, each component being a phase. It provides a definition of the order parameter as being the best variable to separate the two maxima of the distribution. When a nuclear system is in the coexistence region, the probability distribution of an order parameter is bimodal and large fluctuations in the partitions of the system can be observed [35–37]. Experimentally, the width of the Asym_{123} fluctuations, seen in Fig. 10(b), represents about 2/3 of the whole asymmetry distribution. Moreover, the bimodality of the event distribution can be seen in Fig. 9, between the events well reproduced by the SMM model and those well reproduced by the GEMINI model. Hence, the Asym_{123} variable can mimic an order parameter since it shows a two-bump distribution separating two decay processes. Nevertheless, it is likely that other variables could be defined in order to obtain a better separation. Such complementary analyses are required.

VI. SUMMARY AND CONCLUSIONS

In this paper, we focused on the characterization of a single-source sample from ^{58}Ni+^{58}Ni collisions at 32 MeV/nucleon, using a set of complete events recorded by the multidetector INDRA. The high performance of this 4π device and the quality method of event selection have led to a large set of well-characterized data. Indeed, the original discriminant analysis procedure, involving multivariate moments, definitely proved to be an efficient tool to clearly disentangle a single-source contribution from more dominant binarylike dissipative collisions. The four selected cuts investigated (from pure single-source events to pure polysource events) revealed in each case a relatively high energy dissipation. Moreover, a continuity was observed as a function of the appropriate d_{625} discriminant variable between the former and the latter for static and kinematic variables.

The fusionlike subsystem undergoes a statistical multiple-fragment decay after thermal equilibrium is reached. The role of the preequilibrium emission has been investigated. First, about 16 mass units are ejected, i.e., about 14% of the total incident mass. Then, a large part of the initial mass is stored in the subsystem with a mean charge lying around $Z_{\mathrm{tot}} \sim 49$ charge units. On the other hand, the preequilibrium emission leaves nearly half of the convertible energy stored in the subsystem. Nevertheless, its excitation energy corresponds to about 5 ± 0.8 MeV/nucleon which involves a hot subsystem close to the prompt multifragmentation onset.

Surprisingly, events with a large charge asymmetry (≈0.8) still exist and are well accounted for by a statistical sequential decay model (GEMINI). It represents at most 10% of the single-source events. The dominant remaining class of events spread around smaller charge asymmetries (∼0.6) is well reproduced by a statistical simultaneous multifragmentation model (SMM). This coexistence characterizes the transition region from the standard fusion-evaporation process, which is supposed to leave a final heavy cold residue plus light fragments and/or particles, toward a thermal prompt multifragmentation scenario producing fragments of more similar sizes.

Moreover, this duality between a pure evaporative component and a thermal prompt multifragmentation scheme is clearly evidenced for the first time in a medium-size system. For the clean single-source selection obtained, which favors the more asymmetric partitions, no radial expansion energy is needed to accurately reproduce the data, and quite the same excitation energy is stored by both class events. Hence, this duality can be mimicked as a bimodality of the event distribution, each component being a phase. In this scheme, the Asym_{123} variable can be seen as an order parameter. Moreover, the large Asym_{123} fluctuations, observed in the partition of the system, also support the hypothesis of an order parameter.

To improve our knowledge on how this steady competition evolves between these two decay mechanisms, complementary studies at incident energies around 30 MeV/nucleon are required. Of special interest is the analysis of the 40 MeV/nucleon ^{58}Ni+^{58}Ni INDRA data, and even of the higher energy data, presently in progress. These studies should reveal the robustness of the order parameter to sign, in a symmetric medium-size system, a first-order phase transition.

[1] D. Durand, E. Suraud, and B. Tamain, *Nuclear Dynamics in the Nucleonic Regime*, Series in Fundamental and Applied Nuclear Physics (Institute of Physics, Bristol/Philadelphia, 2001), and references therein.

[2] A. M. Maskay, Ph.D. thesis, Université de Lyon, LYCEN T 9969, 1999 (http://tel.ccsd.cnrs.fr/documents/archives0/00/00/72/80).

[3] N. Marie and INDRA Collaboration, Phys. Lett. **B391**, 15 (1997).

[4] M. T. Magda *et al.*, Phys. Rev. C **53**, 1473 (1996).

[5] E. Colin *et al.*, Phys. Rev. C **61**, 067602 (2000); R. Sun *et al.*, *ibid.* **61**, 061601 (2000); Phys. Rev. Lett. **84**, 43 (2000).

[6] B. Borderie and INDRA Collaboration, in International Symposium on Advances in Nuclear Physics, Bucharest, 1999 (unpublished); A. Fhali *et al.*, Phys. Rev. C **34**, 161 (1986); P. F. Box *et al.*, *ibid.* **50**, 934 (1994).

[7] E. Colin *et al.*, Phys. Rev. C **57**, 1032 (1998).

[8] D. Durand, Nucl. Phys. **A630**, (1998) 52c, and references therein.
[9] J. D. Frankland, Ph.D. thesis, Université de Paris XI Orsay, IPNO T 98 06, 1998; Nucl. Phys. **A689**, 905 (2001); **A689**, 940 (2001).
[10] M. D'Agostino *et al*., Nucl. Phys. **A650**, (1999) 329, and references therein.
[11] M. F. Rivet and INDRA Collaboration, Phys. Lett. **B430**, 217 (1998).
[12] P. Eudes *et al*., Phys. Rev. C **56**, 2003 (1997).
[13] M. Germain and INDRA Collaboration, Phys. Lett. **B488**, 211 (2000); Ph.D. thesis, Université de Nantes, 1997.
[14] G. Rudolf *et al*., Phys. Lett. **B307**, 287 (1993).
[15] P. Désesquelles *et al*., and INDRA Collaboration, Phys. Rev. C **62**, 024614 (2000).
[16] J. Pouthas *et al*., Nucl. Instrum. Methods Phys. Res. A **357**, 418 (1995).
[17] P. Désesquelles, Ann. Phys. (Paris) **20**, 1 (1995) (in English).
[18] D. Durand, Nucl. Phys. **A541**, 266 (1992).
[19] A. D. Nguyen, Ph.D. thesis, Université de Caen, LPCC T 9802, 1998.
[20] A. Schüttauf and ALADIN Collaboration, Nucl. Phys. **A607**, 457 (1996).
[21] R. Bougault *et al*., in *Proceedings of the XXVII International Workshop on Gross Properties of Nuclei and Nuclear Excitations*, Hirschegg, edited by H. Feldmeier (GSI, Darmstadt, 1999), p. 24; W. Neubert and A. S. Botvina, Eur. Phys. J. A **7**, 101 (2000).
[22] P. Sapienza *et al*., Phys. Rev. Lett. **87**, 072701 (2001).
[23] D. Doré *et al*., Phys. Rev. C **63**, 034612 (2001).
[24] P. Désesquelles *et al*., Multics/Miniball Collaboration, Nucl. Phys. **A633**, 547 (1998); J. C. Steckmeyer and INDRA Collaboration, *ibid*. **A686**, 537 (2001).
[25] M. Blann, Phys. Rev. C **31**, 1245 (1985).
[26] A. Bonasera *et al*., Phys. Rep. **243**, 1 (1994).
[27] D. Cussol *et al*., Nucl. Phys. **A561**, 298 (1993).
[28] M. Colonna, Ph. Chomaz, and A. Guarnera, Nucl. Phys. **A613**, 165 (1997).
[29] R. J. Charity *et al*., Nucl. Phys. **A483**, 371 (1988).
[30] P. Désesquelles, J. P. Bondorf, A. Botvina, and I. Mishustin, Nucl. Phys. **A604**, 183 (1996).
[31] B. Guiot, Ph.D. thesis, Université de Caen, 2002.
[32] J. P. Bondorf *et al*., Phys. Rep. **257**, 133 (1995).
[33] S. Salou, Ph.D. thesis, Université de Caen, GANIL T 9706, 1997.
[34] N. Bellaize *et al*., Nucl. Phys. **A709**, 367 (2002).
[35] Ph. Chomaz, F. Gulminelli, and V. Duflot, Phys. Rev. E **64**, 046114 (2001).
[36] B. Borderie, J. Phys. G: Nucl. Part. Phys. **28**, 217(R) (2002).
[37] R. Botet *et al*., Phys. Rev. Lett. **86**, 3514 (2001).